Accepted in ***Composites Science and Technology***, 24-02-2021

Effects of Ferromagnetic & Carbon-Fibre Z-Pins on the Magnetic Properties of Composites

Mudan Chen[a], Bing Zhang[a,*], Sven Friedemann[b], Giuliano Allegri[a], Stephen R. Hallett[a]

[a] *Bristol Composites Institute (ACCIS), University of Bristol, Bristol BS8 1TR, United Kingdom*

[b] *HH Wills Laboratory, University of Bristol, Bristol BS8 1TL, United Kingdom*

Graphical Abstract

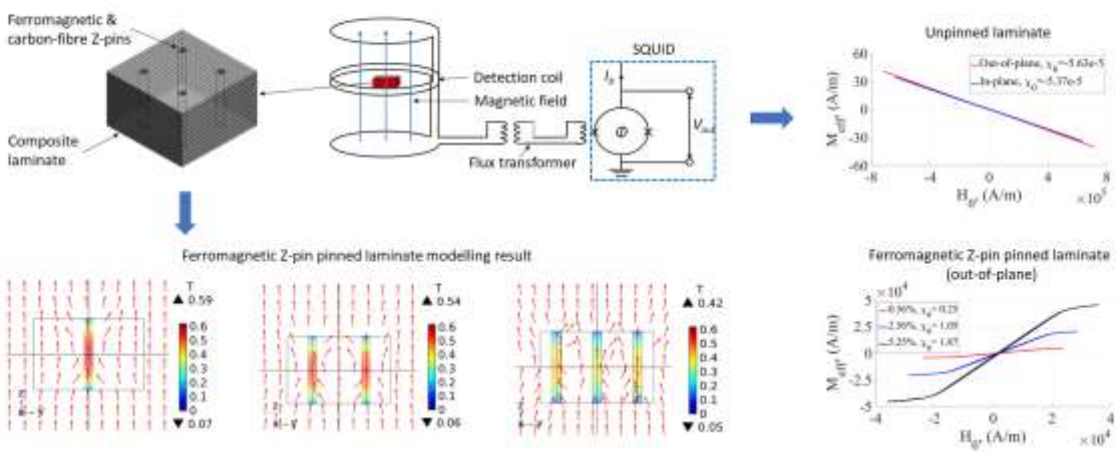

*Corresponding author email address: b.zhang@bristol.ac.uk (Bing Zhang)

Accepted in ***Composites Science and Technology***, 24-02-2021

Effects of Ferromagnetic & Carbon-Fibre Z-Pins on the Magnetic Properties of Composites

Mudan Chen[a], Bing Zhang[a,*], Sven Friedemann[b], Giuliano Allegri[a], Stephen R. Hallett[a]

[a] *Bristol Composites Institute (ACCIS), University of Bristol, Bristol BS8 1TR, United Kingdom*

[b] *HH Wills Laboratory, University of Bristol, Bristol BS8 1TL, United Kingdom*

Abstract

This paper investigates for the first time the effects of Z-pins on the magnetic properties of composite laminates. In-plane and out-of-plane M-H curves of IM7/8552 laminates with and without Z-pins have been characterised by an MPMS3 SQUID magnetometer. Two kinds of pin materials (T300/BMI composite and ferromagnetic Ni/Fe alloy) have been studied at three different volume fractions (nominally 0.5%, 2% and 4%). The unpinned and carbon-fibre pinned laminates were found to be diamagnetic. The carbon-fibre pin had no significant influence on the global magnetic properties of the laminates. The Ni/Fe alloy pin increased the laminate linear-part magnetic volume susceptibility up to 1.87 and 0.13 for the out-of-plane and in-plane directions, respectively. Numerical modelling has been conducted to support the investigation of the effect of the pin volume fraction on the overall magnetic susceptibility and saturation magnetisation. The laminate out-of-plane susceptibility exhibits a nonlinear behaviour dependent on pin volume fraction, due to interactions between adjacent pins. The saturation magnetisation is proportional to the pin volume fraction and independent of field direction.

Keywords: A. Multifunctional composites, A. Laminate, B. Magnetic properties, C. Finite Element Analysis (FEA), Z-pin

1 Introduction

Fibre-reinforced plastic (FRP) laminates have outstanding in-plane performance, but relatively weaker out-of-plane properties. Z-pinning has been developed as an effective through-thickness reinforcement (TTR) technology [1], along with stitching [2], tufting [3], 3D weaving [4], etc. A considerable amount of work has been reported in the literature regarding the mechanical reinforcement function of Z-pins [5–11]. More recently, there has been a strongly growing interest towards the exploration of multi-functionality in composites, in addition to load bearing functions. A number of studies have been published regarding the multi-functionality of Z-pinned composites [12–20].

Zhang et al. [12] characterised the Mode I & Mode II delamination self-sensing function of Z-pinned laminates by measuring the real-time through-thickness electrical resistance for both conductive and non-conductive fibre-reinforced plastics. They later extended the delamination monitoring method to composites reinforced by conductive Z-pin arrays and proposed a structural-level design strategy for multifunctional Z-pinned composites [13]. The latter is based on connecting Z-pins both in series and in parallel via arrays of electrodes attached to the laminate surface. Pegorin et al. [14] experimentally evaluated the effects of pin material (carbon FRP and metals) and volume content on the in-plane and through-thickness electrical conductivities at a coupon scale. It was found that the through-thickness conductivity linearly increased with pin volume content for all materials, and it was enhanced by a factor up to 10^6 by copper Z-pins with a volume fraction of 1.84%. Pegorin et al. [15] also proposed a Mode I delamination monitoring approach for laminates with Z-pin arrays. The electrical resistance between top and bottom electrodes that were attached in unpinned regions was found to increase with delamination length. Compared with unpinned laminates, the resistance change of Z-pinned coupons due to delamination was much larger, thus potentially enabling a versatile and robust monitoring of in-service damage. Grigoriou et al. [16] later extended the electrical-based applications of Z-pins to sandwich composites. In the research of Kadlec et al. [17], Z-pins were found to effectively increase crack arrest ability of adhesive-bonded composite lap joints by 33% under static load. At the same time, the electrical resistance across pins was observed to have the same trend as crack growth, making this approach a promising candidate for structural health monitoring, thus supporting the certification of adhesive-bonded joints in aerospace applications.

By taking advantage of Z-pins combined with graphite sheets, Li et al. [18] developed a structure with a 3D enhanced thermal conductivity. It was found that 2.7% areal density of Z-pins enhanced the through-thickness and in-plane thermal conductivities by 215% and 115%, respectively, compared with unpinned graphite sheet composites. Through FE modelling, Pegorin et. al [19] found that the through-thickness thermal properties of Z-pinned composites could be tailored via pin volume fraction and the appropriate down-selection of pin materials, akin to the through-thickness electrical properties. With the pins acting as the thermal pathways, the through-thickness thermal conductivity grew linearly with pin content.

However, there is still a lack of studies regarding the effects of Z-pins on the magnetic properties of composites. Traditional FRP composites are magnetically inert: they do not show any remnant magnetism and only negligible enhancement of the relative magnetic permeability [21]. The weaker magnetic properties of composites compared to other materials represent an important limitation in several applications (e.g. in electromagnetic machines) [22,23]. For instance, the rotor containment sleeves of a permanent magnet machine are normally made of carbon/glass FRP composites or weak-magnetic metals for load bearing. This generates a large non-magnetic gap between the stator and the magnet, significantly reducing the resulting electromagnetic force. Yon et al. [22] designed a magnetically semi-permeable sleeve to overcome this drawback. Based on an analytical model, they estimated that an optimum relative magnetic permeability ($\mu_r = 7.2$) could increase the fundamental component of the air-gap flux density by 28%. A prototype machine with the sleeve made from cold-rolled 304L stainless steel ($\mu_r \approx 2$) was manufactured and tested. It showed a 20% increment of the electromotive force compared to the magnetically inert material. However, the stainless steel had a low resistivity and needed to be incorporated into a laminated assembly, making the manufacture complex and expensive. With the same purpose, Edwards et al. [23] incorporated magnetic particles into composites by employing epoxy resin film loaded with pure iron particles into laminates. By embedding one film between every adjacent ply (8 plies, 7 films), the predicted relative permeability was improved, whilst the ultimate tensile strength was reduced to 60%.

Besides electromagnetic machines, Etches et al. [24] demonstrated how tailoring the magnetic properties of composites can be potentially used for magnetic actuation of the trailing edge of a morphing aerofoil. Two magnetic materials (barium ferrite and ferrofluids) were separately embedded into hollow glass fibres. Due to the particle size and viscosity, the maximum achievable volume fraction of barium ferrite was only 3%. For ferrofluids, the filler volume fraction reached 30%. The ferrofluids-filled coupon was successfully actuated in an applied magnetic field.

Compared with the methods for improving the magnetic properties of composites reviewed above, Z-pinning offers a relatively wider material selection range, since Z-pins can be in principle made of any material that can be processed into small rods. Similar to the research on electrical and thermal properties of Z-pinned composites in [12,14,18], this study also places emphasis on the effects of Z-pins on the global physical properties of composites. Meanwhile, some local meso-scale analyses are also presented to better understand the global effects observed. Specimen preparation and experimental set-up are introduced in Section 2 and Section 3. The magnetic properties of single Z-pins (not inserted into a composite laminate) are first characterised in Section 4. Experimental results for Z-pinned laminate samples are then presented in Section 5. The influence of pin misalignment and volume fraction on the magnetic susceptibilities of through-thickness reinforced composites in both the in-plane and out-of-plane directions are discussed in Section 6.

2 Specimen preparation

Metallic and carbon FRP Z-pins have been widely characterised for their mechanical performance in the literature. 0.25 mm diameter Ni80/Fe20 permalloy pins (from GoodFellow) and 0.28 mm diameter T300/BMI pins (from DPP BV) were considered in this study.

Z-pinned laminate specimens were manufactured employing 16 plies of Hexcel's IM7/8552 carbon/toughened-epoxy prepreg, with a stacking sequence of $[0°/+45°/90°/-45°]_{2s}$. This quasi-isotropic (QI) stacking sequence is a representative configuration for laminates in many structural applications. The maximum sample in-plane diagonal length allowed was 4.8 mm, due to the configuration of the sample holder in the MPMS3 magnetometer. Considering the pin spacing for nominal 0.5%, 2% and 4% volume fractions, the Z-pinned coupons were designed to have the dimensions of

3.1×3.1 ×2 mm. Figure 1 (a) shows the configuration of a 2% pinned coupon as an example.

The manufacturing process consisted of four steps. (1) The prepreg was defrosted for 2 hours and laid up to form the laminate, with de-bulking after every four plies. (2) The carbon-fibre pins were cut from a protruded rod stock and the alloy pins were cut from a wire roll with scissors; then both types of Z-pins were manually inserted into the uncured laminate. (3) The Z-pinned laminate was cured in an autoclave, following the cycle recommended by Hexcel [25]. (4) Finally, the coupons were carefully cut from the cured laminate using a water-cooled diamond-coated saw.

3 Experimental set-up

A SQUID (Superconducting Quantum Interference Device) magnetometer model MPMS3 manufactured by Quantum Design was used in DC scan mode in this research (Figure 1 (b)). The SQUID DC mode measures directly the magnetic flux of the sample utilizing the Josephson effect, which employs interference of the wave function around a superconducting loop where the magnetic flux of the sample is coupled in via a flux transformer. Usage of gradiometer coils removes the signal from the applied magnetic field, allowing to detect the magnetic flux from the sample as the sample is moved through the gradiometer. From the measurement of the flux as a function of position in the gradiometer, the magnetic moment of the sample is extracted using the MPMS3 software calibrated on a palladium standard [26,27]. A simplified schematic of the measurement system is drawn in Figure 1 (c), with the SQUID highlighted in the dashed green box, in which I_b is the bias current, Φ is the flux threading the SQUID, and V_{out} is the voltage responding to the flux. The magnetic field in the MPMS3 is generated by a superconducting electromagnet.

As shown in Figure 1 (b), the applied magnetic field was always in the vertical direction. For the axial direction tests, a single z-pin (not inserted into the composite) was glued on a quartz rod with a semicircle cross section and the pin axis was aligned with the magnetic field direction. For the radial and angled pin tests, due to the pin tending to align itself with the applied magnetic field, it was inserted into a fixed nylon holder, to eliminate any rotation. The magnetic field was along the pin radius direction for radial tests, and there was an angle between the magnetic field and pin axis for the angled pin tests.

The Z-pinned laminate coupons were glued onto the nylon support cylinder and put into a capsule. Nylon contributes a negligible background signal as its permeability deviates less than 10^{-5} from that of free space [28], i.e. $1 < \mu_r < 1 + 10^{-5}$. The magnetic field was applied along the 0° ply fibre direction (X axis) for the in-plane measurements, whilst the magnetic field was along the specimen thickness direction (Z axis) for the out-of-plane measurements.

In order to get a full M-H loop, the applied magnetic field H_0 was increased linearly from zero to a field $H_{\max}$ sufficient to observe magnetisation saturation, then decreased to $-H_{\max}$, and finally brought back to $H_{\max}$. The total duration of one scan was 1.5 to 2 hours. Each scan was repeated twice to ensure the reliability of data.

4 Single pin results

In the experiments, the total magnetic moment of a sample was measured and converted into an effective magnetisation using the measured sample volume. All the M-H curves shown below present this effective magnetisation M_{eff} against the external field H_0. Note that the magnetisation is nonuniform inside the sample as we show later in detail in the simulations. The effective magnetic susceptibility χ_0 of the tested samples is extracted from linear fitting in the low-field regime of the M-H curve. From this point, the low-field relative permeability is calculated as $\mu_r = \chi_0 + 1$.

4.1 Carbon-fibre FRP pins

In the DC SQUID option, a resolution of 10^{-9} A·m^2 is achieved by measuring a gel capsule in a straw with the standard setup. For an individual carbon pin with its small volume (diameter: d = 0.28 mm, length: l = 4 mm), however, the magnetic moment is too small to be detected. This is consistent with the expected magnetic moment $m \approx 7 \times 10^{-11}$ A·m^2 in a field of $\mu_0 H_0 = 0.1$ T for a sample of this size containing pure graphite [29] .

4.2 Ni/Fe pins

4.2.1 Susceptibility vs. length

Firstly, the effect of cure on the Ni/Fe Z-pin magnetic properties can be ignored, which was confirmed by testing a pin before and after curing and observing that the resulting M-H curves were the same.

The intrinsic magnetic permeability of Ni80/Fe20 permalloy is quite high [30], however, in a finite size volume, the effects of demagnetisation give rise to a complex variation of magnetisation M across the volume and hence the magnetic moment has a non-linear dependence on magnetic field. In some limited cases, the demagnetizing factor N can be used to obtain the internal field H as $H = H_0 - NM$. As reported [31,32], the demagnetizing factor N of a cylinder is a complex function of the susceptibility and ratio of length to diameter as well as the orientation of the magnetic field. In small magnetic fields, a linear dependence can be approximated using the demagnetizing factor N depending on the sample shape and orientation in magnetic field only [33]. In this work the non-linear regime was also studied and finite element analysis was used to model the behaviour of the samples, as analytical expressions are not available.

Since the Ni/Fe pin has a constant diameter of 0.25 mm, pins with lengths ranging from 1.5 to 4.1 mm in both the axial and radial directions were characterised. The experimental single-pin M-H curves are plotted in Figure 2 (a, b). The slightly horizontal offset of the M-H curves is most likely due to the remnant field in the superconducting magnet following previous measurements at large magnetic fields.

For both directions, the magnetisation initially increases linearly with the applied magnetic field H_0, then, following a nonlinear response stage, it quickly reaches saturation. The curves also reveal the very soft ferromagnetic behaviour of these permalloy pins, as they have narrow hysteresis loops with very small coercive field and remanence [30]. For the axial orientation, the slope of the low-field linear regime is larger for longer samples and the non-linear response is shifted to lower fields for longer samples, while the radial M-H behaviour is almost coincident for all samples. The saturation magnetisation M_s is independent of pin length for both directions.

For a quantitative analysis, the low-field susceptibilities are plotted against the pin length in Figure 2 (c, d). This shows that the susceptibility for axial field orientation increases linearly from 21 to 100 with the pin length growing from 1.5 to 4.1 mm. Conversely, the values for radial orientation of the field are much lower, having a mean value of 2.5. In the low-field limit, the magnetic behaviour of the alloy pins can be captured as that of a cylinder in an axial field with a demagnetizing factor, in agreement with the linear M-H curve seen in the measurements at low fields. The demagnetizing factor N_z decreases with the length to diameter ratio in agreement with the increased effective susceptibility found in these measurements [31,32]. At the same time, the demagnetizing factor N_x relating with the radially applied magnetic field is much higher than N_z for a long thin cylinder [34] and relatively independent of the pin length, in agreement with the experimental results.

4.2.2 Susceptibility vs. inclination angle

Since pin misalignment is a common and unavoidable manufacturing feature in Z-pinned laminates, the effect of the inclination angle α (the angle between pin axis and magnetic field) is explored. The out-of-plane misalignment angle usually varies between 5° and 20° [35]. A 4.05 mm Ni/Fe pin was tested at pre-defined 0°, 20°, 40°, 60°, 70° and 90° inclination angles with an accuracy of ±2°.

The experimental M-H curves are plotted in Figure 3 (a). The curves show a decrease of the initial slope and increase of the saturation field as the inclination angle increases, whilst the saturation magnetisation remains independent on the angle. The calculated saturation flux density B_s is around 1.1 T, which is consistent with the data for 80% nickel permalloy from literature [30]. The low-field susceptibilities are extracted and plotted in Figure 3 (b) as a function of the inclination angle. A nonlinear decrease trend is observed as the inclination angle increases.

5 Laminate results

5.1 Unpinned laminate

The individual sample dimensions for the unpinned carbon fibre reinforced plastic (CFRP) coupons were 3.2 mm × 3.1mm × 2.0 mm. Since the laminate has a quasi-isotropic stacking sequence, it is expected to exhibit negligible differences in magnetic properties for any arbitrary in-plane direction.

The out-of-plane and in-plane M-H curves of the unpinned specimen are plotted in Figure 4 (a). They present linear decreasing trends, and no saturation and hysteresis were observed even at much higher H_{max} values than those employed in the characterisation of alloy Z-pins. This confirms that the CFRP considered here is a weakly diamagnetic material [36]. The in-plane and out-of-plane M-H curves almost coincide, with susceptibility values of -5.37×10^{-5} and -5.63×10^{-5}, respectively.

5.2 Carbon-fibre Z-pin pinned laminate

Three carbon-fibre Z-pin pinned coupons with different pin volume fractions were tested. The actual volume fractions were calculated at 0.51%, 2.00% and 4.46%, by accurately measuring the specimen dimensions and the pin length (including the small amount of protruding top and bottom).

The in-plane and out-of-plane M-H curves are plotted in Figure 4 (b), with the corresponding susceptibilities χ_0 listed in the legend. Similar to the case of the unpinned CFRP, all curves present small monotonically decreasing trends, which implies that carbon Z-pinned laminates are also diamagnetic in both in-plane and out-of-plane directions. It appears that the absolute value of the susceptibility decreases with the pin volume fraction for both directions. The out-of-plane susceptibility is quite close to that of the in-plane direction. Compared with unpinned CFRP (i.e., comparing Figure 4 (a) and (b)), the carbon fibre Z-pin reinforced coupons present effective susceptibilities with the same order of magnitude as for unpinned CFRP. This proves that carbon fibre pins have no large influence on the global magnetic susceptibility of a CFRP laminate.

5.3 Ni/Fe Z-pin pinned laminate

The actual pin volume fractions for the samples reinforced with alloy pins were measured at 0.56%, 2.56% and 5.25%, respectively. The corresponding experimental M-H curves are plotted in Figure 4 (c, d). The curves have similar trends to those for the single Ni/Fe pin tests. The saturation magnetisation M_s increases with the pin volume fraction for both in-plane and out-of-plane directions. Similar to the results on single alloy pins, M_s is independent from the field direction for a given pin volume fraction (i.e. comparing the same-colour curves in Figure 4 (c) and (d)).

As shown in the legends of Figure 4 (c, d), low-field effective susceptibilities in the linear response region for the 0.56%, 2.56%, 5.25% pinned samples are 0.25, 1.05, 1.87 (out-of-plane) and 0.01, 0.07, 0.13 (in-plane), respectively. Compared with the diamagnetic unpinned coupon, the laminate with Ni/Fe Z-pins become strongly paramagnetic, with large susceptibilities. The low-field susceptibilities against pin volume fractions are plotted with solid lines in Figure 4 (e) and (f). For comparison, the dashed trend lines in Figure 4 (e) and (f) are given by the rule of mixtures:

$$\chi_{0\_\text{sample}} = \left(1 - V_{\text{f\_pin}}\right) \cdot \chi_{0\_\text{lam}} + V_{\text{f\_pin}} \cdot \chi_{0\_\text{pin}} \tag{1}$$

where χ_{0_sample}, χ_{0_lam} and χ_{0_pin} are the effective susceptibilities of pinned sample, unpinned laminate, and pin, respectively. $V_{\text{f\_pin}}$ is the pin volume fraction. Since χ_{0_lam} was measured to be very small for both directions (in the order of 10^{-5}), χ_{0_sample} is dominated by the pin volume fraction and susceptibility. When considering the in-plane behaviour, the experiments and analytical prediction agree well and only exhibit a slight difference for the 2.56% volume fraction sample. However, the difference is more evident for the out-of-plane direction especially at a higher pin volume fraction, which means that the magnetic susceptibility of the pinned samples does not increase linearly to the volume fraction of the soft-ferromagnetic through-thickness reinforcement. This is potentially due to the pin misalignment and interaction, which will be further investigated in the following section with the aid of finite element analysis (FEA).

6 Discussion

Comparing the test results for the unpinned laminate in Section 5.1 and the Ni/Fe Z-pinned laminate in Section 5.3, it can be concluded that the magnetic properties of a ferromagnetic pinned laminate are dominated by the pins. Since in Section 5.2 carbon-fibre pins have been shown to have minor influence on the global magnetic behaviour of composites, only the effects of Ni/Fe pins will be further discussed in this section, considering the effects of pin misalignment, interaction, and volume fraction.

6.1 Pin misalignment effect

As illustrated in the experiments, the saturation magnetisation M_s is independent of the inclination angle (Figure 3 (a)), and pin length (Figure 2 (a, b)). It has also been demonstrated in Figure 4 (c) and (d) that M_s increases with pin volume fraction. Thus, M_s will also increase with pin misalignment since the latter leads to a larger pin volume fraction in a fixed thickness laminate with the pins running the full thickness.

The misalignment influences the low-field susceptibility of a Z-pinned laminate in four aspects. Firstly, the effective susceptibility of the laminate will increase due to the increased pin volume fraction caused by misalignment, similar to the saturation magnetisation discussed above. Secondly, the longer pin length due to misalignment will result in a change of the demagnetizing factor in a different way for in-plane and out-of-plane orientations. The growth of pin length due to misalignment results in an apparent increase of the effective susceptibility χ_0 of a single pin for the out-of-plane direction (Figure 2 (c)), while no obvious influence for the in-plane property (Figure 2 (d)). Thirdly, the inclination angle due to pin misalignment has further effects on the demagnetizing factor as shown in Figure 3 (b). For misalignment angle typically within 20° [35], it shows in Figure 3 (b) that the segment of 0° to 20° which corresponds to the out-of-plane direction of Z-pinned laminate only slightly decreases, while the part from 90°-70° related with the laminate in-plane direction has an apparent increment. Fourthly, pin misalignment would change the pin-to-pin distance in three dimensions and thus affect the pin interaction via magnetic field. A systematic study on the effect of pin misalignment will be addressed in a separate study by taking the aforementioned aspects into account.

6.2 Pin volume fraction effect

6.2.1 Numerical modelling

The commercial FEA tool COMSOL Multiphysics® was employed to help explain the influence of pin volume fraction. The magnetic vector potential $\boldsymbol{A}$ is employed as a field variable for the element nodes in the FE models. The following equations are used for the magnetostatics case [37]:

$$\nabla \cdot \boldsymbol{B} = 0 \tag{2}$$

$$\boldsymbol{B} = \nabla \times \boldsymbol{A} \tag{3}$$

$$\boldsymbol{B} = \mu_0(\boldsymbol{H} + \boldsymbol{M}) \tag{4}$$

where μ_0 is the vacuum permeability. The modelling strategy is verified through the alloy pin and pinned laminate tests as presented in Sections 4.2 and 5.3.

Each of the verification models consisted of the coupon (single pin or pinned laminate) in the middle of a relatively large free-space sphere and a layered infinite empty domain outside, as shown in Figure 5 by taking the 3 by 3 pin embedded laminate as an example. When modelling the tested Ni/Fe Z-pinned coupons, the pin misalignment must be considered since it affects the magnetic properties of composites as discussed in Section 6.1. To measure the pin misalignment, the sample top and bottom surfaces were scanned with a microscope, then each pin was located from the scanned photos. Pin misalignment angles were determined by the distance between pin ends and sample edges. For the 1-pinned, 4-pinned and 9-pinned samples, the average misalignment angles are calculated as 9.1°, 8.4°, 6.3° respectively. Tetrahedral elements were employed throughout the whole mesh. For all the models presented here, mesh convergence studies have been conducted. There are 32 elements along the top or bottom circle and 16 elements per/mm in the length direction. A uniform background magnetic field was applied, which is consistent with the experimental set-up. The B-H curve of 80% nickel permalloy (Figure 6) from the COMSOL nonlinear magnetic material library [38] was used for the pin in the simulation. The material data in COMSOL originates from the MagWeb database [39].

The modelling verification results are presented in the supplementary material. It shows that good agreement between experimental measurements and modelling predictions is obtained, and minor discrepancies only arise in the transition region for 60° and 70° angled pins. These differences could be attributed to the following factors. Firstly, the pins are modelled as a cylinder, while the real pin end shape is not perfectly flat after being cut with scissors. In addition, during the manufacturing process of wire such as pull-out, the grain texture inside the wire might be changed, which might influence the magnetic anisotropy and anisotropy of domain wall movements. Such magnetic anisotropy was not taken into account in the modelling. However, the overall simulation results are consistent with the experiments, especially for the most interesting linear and plateau regions of the response. The FEA also allows observing the flux density distribution inside pins, as shown in Figure 7 for the tested Ni/Fe Z-pinned coupons.

6.2.2 Model results discussion

In order to study the volume fraction effect, three ideal coupons (all having 3.1 ×3.1 ×2 mm^3 dimensions) respectively comprising 1, 4 and 9 pins were modelled with all the pins perfectly straight, without protruding parts.

The linear-region susceptibility versus pin volume fraction curves of the three models are plotted in Figure 8 (a, b). Similar with the experimental findings reported in Figure 4 (e, f), the out-of-plane curves from the simulations present a clearly nonlinear trend and it does not follow the rule of mixture in Figure 8 (a). On the other hand, the rule of mixture gives good results for the in-plane curves, as seen in Figure 8 (b).

To understand this, the cross-section flux distribution given in Figure 9 must be considered. For easy comparison, the colour bar ranges were set equal for each direction, and the maximum and minimum flux values are listed beside the triangle symbols in the graphs. For a single pin in the axial direction (out-of-plane), the flux is maximal at the pin centre (Figure 9 (a)) due to the focusing of flux by the high permeability of the material. In the radial direction, the flux is homogeneous over most of the pin with a small increase at the ends (Figure 9 (d)).

For multiple pins, the flux density from the external field is distributed over several pins and thus limits the enhancement of magnetisation compared to the case of a single pin. Furthermore, the extent of this flux sharing increases with the pin volume fraction and decreases with the pin spacing (comparing Figure 9 (b) and (c)). There are no observable interactions between pins when the magnetic field is applied transversely, and the flux density and distribution inside each pin show no significant dependence on pin volume fraction.

The saturation magnetisation M_s as a function of pin volume fraction is plotted in Figure 8 (c). This shows that the M_s is proportional to volume fraction for both directions and independent from the magnetic field direction, as the in-plane and out-of-plane curves completely coincide. This is simply because the pin volume fraction determines the number of atomic magnetic moments per unit volume. The observation also explains the experimental results for Ni/Fe pinned coupons reported in Section 5.3.

7 Conclusions

The magnetic properties of Z-pinned CFRP laminates have been investigated experimentally and numerically. Several conclusions could be drawn here:

1) Carbon-fibre Z-pins do not have large influence on the global magnetic properties of composites. 2) Soft ferromagnetic Ni/Fe Z-pins lead to a much larger magnetic susceptibility in the axial direction than in the radial one. 3) Ni/Fe pins enhance the laminate out-of-plane and in-plane low-field linear-region effective susceptibilities up to 1.87 and 0.13 at 5.25% volume fraction, respectively. 4) The low-field linear-region effective susceptibility of Ni/Fe pinned laminate increases with pin volume fraction nonlinearly due to pin interactions for the out-of-plane direction, but linearly for the in-plane orientation. 5) The global saturation magnetisation is only dependent on pin volume fraction and independent from field direction.

In summary, it is feasible to tailor the magnetic properties of composites through controlling the volume fraction of ferromagnetic pins. Embedding ferromagnetic through-thickness reinforcement in FRP laminates can widen the application range of FRP composites in electromagnetic applications.

CRediT authorship contribution statement

Mudan Chen: Methodology, Validation, Formal analysis, Investigation, Writing - Original Draft. **Bing Zhang:** Conceptualization, Methodology, Validation, Formal analysis, Investigation, Resources,

Writing - Review & Editing, Supervision, Project administration. **Sven Friedemann:** Methodology, Validation, Formal analysis, Investigation, Resources, Writing - Review & Editing, Supervision. **Giuliano Allegri:** Conceptualization, Formal analysis, Writing - Review & Editing, Supervision. **Stephen R. Hallett:** Conceptualization, Formal analysis, Resources, Writing - Review & Editing, Supervision.

Declaration of Competing Interest

None

Acknowledgements

This work was supported by the Engineering and Physical Sciences Research Council (EPSRC) through the Centre for Doctoral Training in Advanced Composites for Innovation and Science (grant number EP/L016028/1). The COMSOL license was supported by the Bristol University CAME School Pump-Primping fund 2019. We are also grateful for advice given by Prof. Walther Schwarzacher and Dr Dmitry S. Ivanov on data analysis, Dr Chrystel Remillat, Dr Kate Gongadze and Dr Robert Hughes on simulations, as well as Mr Israel Osmond and Dr Mengze Zhu on experiments.

References

[1] A.P. Mouritz, Review of z-pinned laminates and sandwich composites, Composites Part A: Applied Science and Manufacturing. 139 (2020) 106128. https://doi.org/10.1016/j.compositesa.2020.106128.

[2] K. Dransfield, C. Baillie, Y.-W. Mai, Improving the delamination resistance of CFRP by stitching—a review, Composites Science and Technology. 50 (1994) 305–317. https://doi.org/10.1016/0266-3538(94)90019-1.

[3] G. Dell’Anno, J.W.G. Treiber, I.K. Partridge, Manufacturing of composite parts reinforced through-thickness by tufting, Robotics and Computer-Integrated Manufacturing. 37 (2016) 262–272. https://doi.org/10.1016/j.rcim.2015.04.004.

[4] R. Gerlach, C.R. Siviour, J. Wiegand, N. Petrinic, In-plane and through-thickness properties, failure modes, damage and delamination in 3D woven carbon fibre composites subjected to impact loading, Composites Science and Technology. 72 (2012) 397–411. https://doi.org/10.1016/j.compscitech.2011.11.032.

[5] F. Warzok, G. Allegri, M. Gude, S.R. Hallett, Experimental study of Z-pin fatigue; understanding of mode I and II coupon behaviour, Composites Part A: Applied Science and Manufacturing. 127 (2019) 105615. https://doi.org/10.1016/j.compositesa.2019.105615.

[6] A.R. Ravindran, R.B. Ladani, C.H. Wang, A.P. Mouritz, Hierarchical mode I and mode II interlaminar toughening of Z-pinned composites using 1D and 2D carbon nanofillers, Composites Part A: Applied Science and Manufacturing. 124 (2019) 105470. https://doi.org/10.1016/j.compositesa.2019.05.038.
[7] M. Li, P. Chen, B. Kong, T. Peng, Z. Yao, X. Qiu, Influences of thickness ratios of flange and skin of composite T-joints on the reinforcement effect of Z-pin, Composites Part B: Engineering. 97 (2016) 216–225. https://doi.org/10.1016/j.compositesb.2016.05.007.
[8] F. Pegorin, K. Pingkarawat, S. Daynes, A.P. Mouritz, Influence of z-pin length on the delamination fracture toughness and fatigue resistance of pinned composites, Composites Part B: Engineering. 78 (2015) 298–307. https://doi.org/10.1016/j.compositesb.2015.03.093.
[9] H. Cui, M. Yasaee, A.R. Melro, Dynamic inter-fibre failure of unidirectional composite laminates with through-thickness reinforcement, Composites Science and Technology. 176 (2019) 64–71. https://doi.org/10.1016/j.compscitech.2019.04.004.
[10] B. M'membe, M. Yasaee, S.R. Hallett, I.K. Partridge, Effective use of metallic Z-pins for composites' through-thickness reinforcement, Composites Science and Technology. 175 (2019) 77–84. https://doi.org/10.1016/j.compscitech.2019.02.024.
[11] J. Hoffmann, G. Scharr, Compression properties of composite laminates reinforced with rectangular z-pins, Composites Science and Technology. 167 (2018) 463–469. https://doi.org/10.1016/j.compscitech.2018.08.042.
[12] B. Zhang, G. Allegri, M. Yasaee, S.R.R. Hallett, I.K.K. Partridge, On the delamination self-sensing function of Z-pinned composite laminates, Composites Science and Technology. 128 (2016) 138–146. https://doi.org/10.1016/j.compscitech.2016.03.019.
[13] B. Zhang, G. Allegri, S.R. Hallett, An experimental investigation into multi-functional Z-pinned composite laminates, Materials and Design. 108 (2016) 679–688. https://doi.org/10.1016/j.matdes.2016.07.035.
[14] F. Pegorin, K. Pingkarawat, A.P. Mouritz, Controlling the electrical conductivity of fibre-polymer composites using z-pins, Composites Science and Technology. 150 (2017) 167–173. https://doi.org/10.1016/j.compscitech.2017.07.018.
[15] F. Pegorin, K. Pingkarawat, A.P. Mouritz, Electrical-based delamination crack monitoring in composites using z-pins, Composites Part A: Applied Science and Manufacturing. 104 (2018) 120–128. https://doi.org/10.1016/j.compositesa.2017.10.025.
[16] K. Grigoriou, R.B. Ladani, A.P. Mouritz, Electrical properties of multifunctional Z-pinned sandwich composites, Composites Science and Technology. 170 (2019) 60–69. https://doi.org/10.1016/j.compscitech.2018.11.030.
[17] M. Kadlec, R. Růžek, P. Bělský, Concurrent use of Z-pins for crack arrest and structural health monitoring in adhesive-bonded composite lap joints, Composites Science and Technology. 188 (2020) 107967. https://doi.org/10.1016/J.COMPSCITECH.2019.107967.
[18] M. Li, Z. Fang, S. Wang, Y. Gu, Y. Li, Z. Zhang, Thermal conductivity enhancement and heat transport mechanism of carbon fiber z-pin graphite composite structures, Composites Part B: Engineering. 172 (2019) 603–611. https://doi.org/10.1016/J.COMPOSITESB.2019.05.092.

[19] F. Pegorin, K. Pingkarawat, A.P. Mouritz, Numerical analysis of the heat transfer properties of z-pinned composites, Composites Communications. 8 (2018) 14–18. https://doi.org/10.1016/j.coco.2018.03.002.
[20] B. Gu, H. Zhang, B. Wang, S. Zhang, X. Feng, Fracture toughness of laminates reinforced by piezoelectric z-pins, Theoretical and Applied Fracture Mechanics. 77 (2015) 35–40. https://doi.org/10.1016/j.tafmec.2015.01.007.
[21] J. Summerscales, Microstructural Characterisation of Fibre-Reinforced Composites, Woodhead Publishing, 1998.
[22] J.M. Yon, P.H. Mellor, R. Wrobel, J.D. Booker, S.G. Burrow, Analysis of semipermeable containment sleeve technology for high-speed permanent magnet machines, IEEE Transactions on Energy Conversion. 27 (2012) 646–653. https://doi.org/10.1109/TEC.2012.2202232.
[23] L.E. Edwards, J.M. Yon, I.P. Bond, P.H. Mellor, Structural magnetic composites for use in electro-mechanical applications, ICCM International Conferences on Composite Materials. 2015-July (2015) 19–24.
[24] J. Etches, I. Bond, P. Mellor, Manufacture and applications of magnetically active fibre reinforced composites, Smart Mater. Struct. 15 (2006) 288–294. https://doi.org/10.1088/0964-1726/15/2/007.
[25] Prepreg Data Sheet | Hexcel, (2020). https://www.hexcel.com.
[26] Magnetic Property Measurement System, MPMS 3 User’s Manual, (2016).
[27] M. Schmelz, R. Stolz, Superconducting Quantum Interference Device (SQUID) Magnetometers, in: A. Grosz, M.J. Haji-Sheikh, S.C. Mukhopadhyay (Eds.), High Sensitivity Magnetometers, Springer International Publishing, Cham, 2017: pp. 279–311. https://doi.org/10.1007/978-3-319-34070-8_10.
[28] S. Hwang, S.-K. Lee, Efficient Experimental Design for Measuring Magnetic Susceptibility of Arbitrarily Shaped Materials by MRI, Investigative Magnetic Resonance Imaging. 22 (2018) 141–149. https://doi.org/10.13104/imri.2018.22.3.141.
[29] J. Heremans, C.H. Olk, D.T. Morelli, Magnetic susceptibility of carbon structures, Phys. Rev. B. 49 (1994) 15122–15125. https://doi.org/10.1103/PhysRevB.49.15122.
[30] D. Jiles, Introduction to Magnetism and Magnetic Materials, CRC Press, 2015.
[31] D.-X. Chen, J.A. Brug, R.B. Goldfarb, Demagnetizing factors for cylinders, IEEE Transactions on Magnetics. 27 (1991) 3601–3619. https://doi.org/10.1109/20.102932.
[32] D.-X. Chen, E. Pardo, A. Sanchez, Fluxmetric and magnetometric demagnetizing factors for cylinders, Journal of Magnetism and Magnetic Materials. 306 (2006) 135–146. https://doi.org/10.1016/j.jmmm.2006.02.235.
[33] X.B. Xu, L. Zeng, Ferromagnetic cylinders in earth’s magnetic field—a two-dimentional model of magnetizaion of submarine, (1998) 17.
[34] M. Sato, Y. Ishii, Simple and approximate expressions of demagnetizing factors of uniformly magnetized rectangular rod and cylinder, Journal of Applied Physics. 66 (1989) 983–985. https://doi.org/10.1063/1.343481.
[35] M. Yasaee, J.K. Lander, G. Allegri, S.R. Hallett, Experimental characterisation of mixed mode traction–displacement relationships for a single carbon composite Z-pin, Composites Science and Technology. 94 (2014) 123–131. https://doi.org/10.1016/j.compscitech.2014.02.001.

[36] A. Galehdar, K.J. Nicholson, P.J. Callus, W.S.T. Rowe, S. John, C.H. Wang, K. Ghorbani, The strong diamagnetic behaviour of unidirectional carbon fiber reinforced polymer laminates, Journal of Applied Physics. 112 (2012) 113921. https://doi.org/10.1063/1.4764041.
[37] R. Prozorov, V.G. Kogan, Effective Demagnetizing Factors of Diamagnetic Samples of Various Shapes, Physical Review Applied. 10 (2018) 1. https://doi.org/10.1103/PhysRevApplied.10.014030.
[38] Multiphysics Simulations Material Library - Adding Material Properties, (2021). https://www.comsol.com/material-library.
[39] Nickel Steel, MAGWEB. (2021). https://magweb.us/product/nickel-steel/.

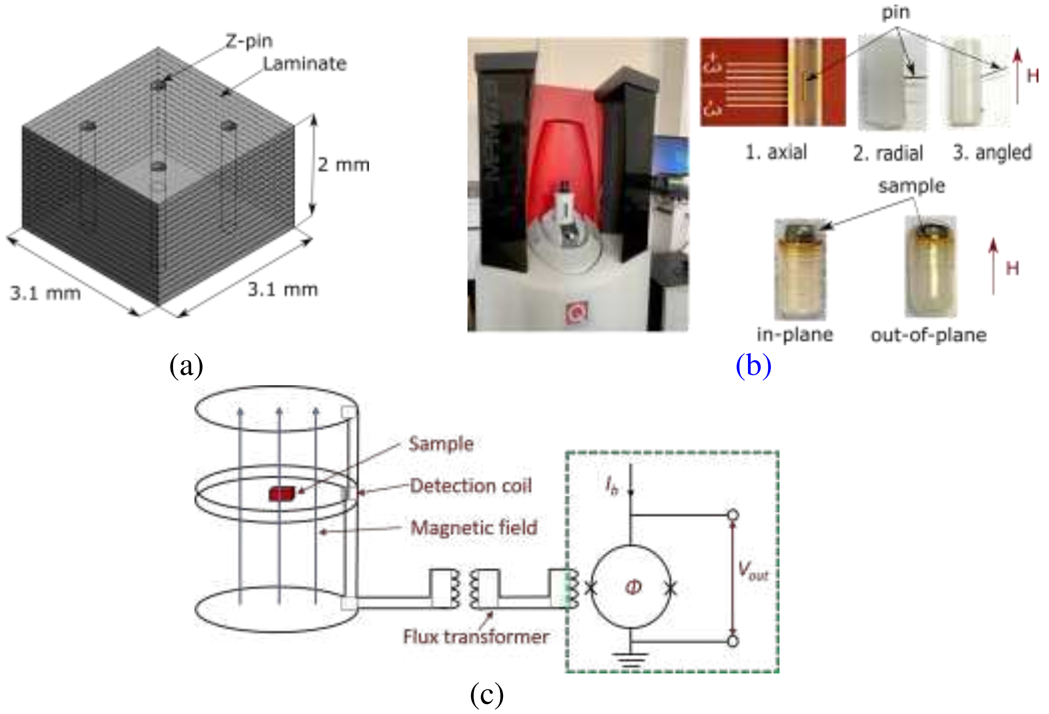

Figure 1. (a) Nominal 2% Z-pinned coupon configuration, (b) SQUID MPMS3 and sample installations, (c) schematic of the SQUID detecting system diagram.

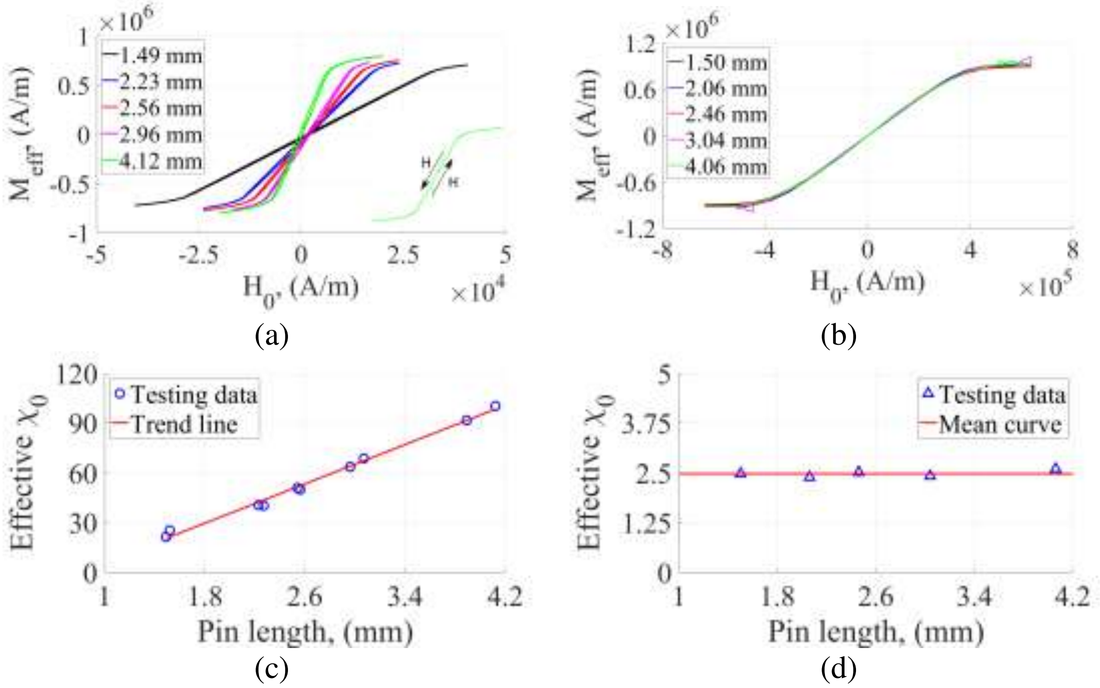

Figure 2. Ni/Fe pin experimental results: (a) axial M-H curves, (b) radial M-H curves, (c) axial linear-part effective susceptibility against pin length, (d) radial linear-part effective susceptibility against pin length.

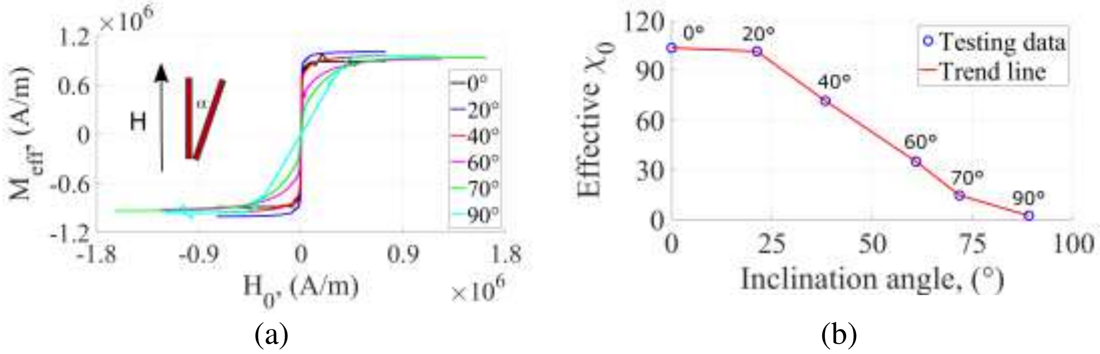

Figure 3. Misaligned Ni/Fe pin experimental results: (a) M-H curves, (b) linear-part effective susceptibility against inclination angle.

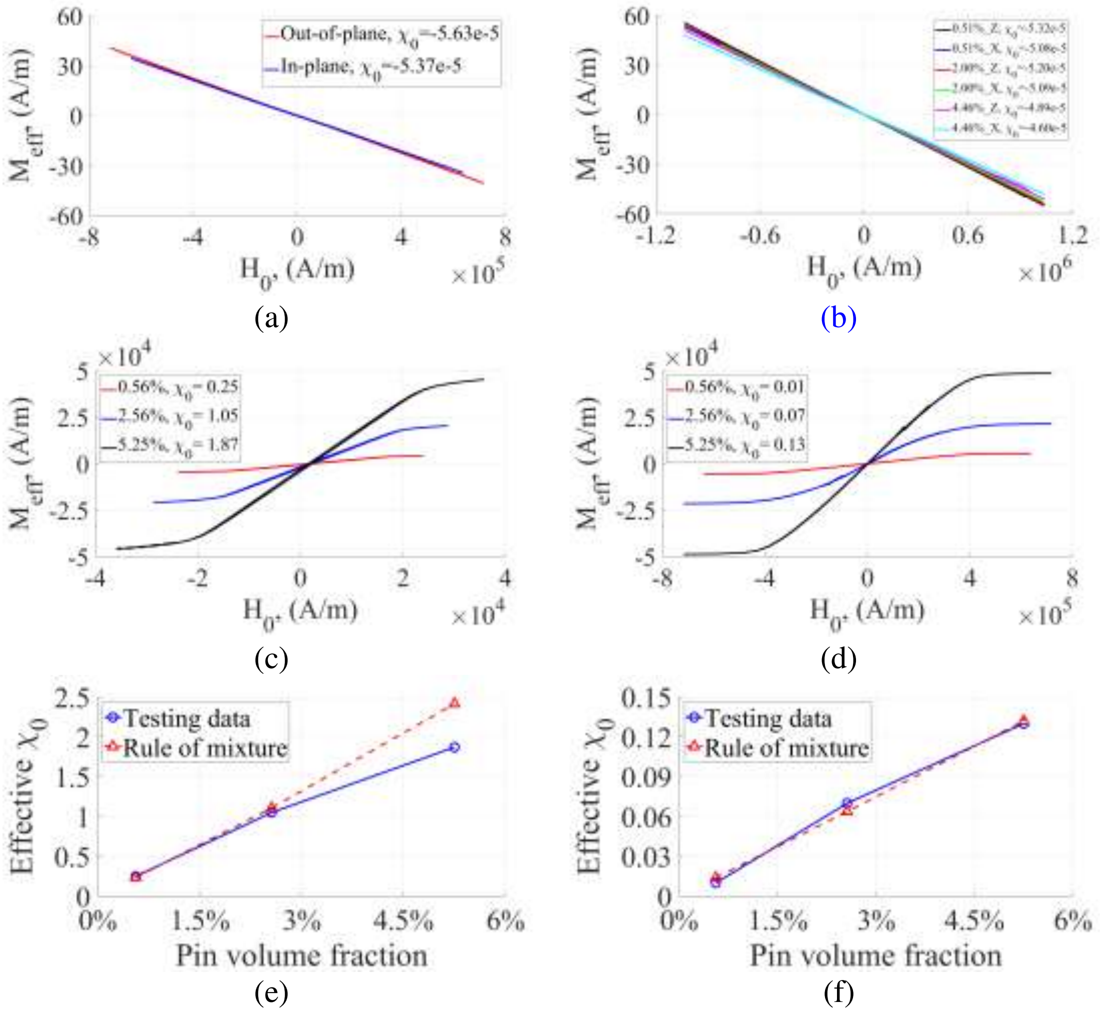

Figure 4. (a) M-H curves of the unpinned sample, (b) M-H curves of carbon FRP Z-pinned samples (out-of-plane: Z, in-plane: X); Ni/Fe Z-pinned samples M-H curves: (c) out-of-plane, (d) in-plane; linear-part effective magnetic susceptibility against the Ni/Fe pin volume fraction: (e) out-of-plane, (f) in-plane

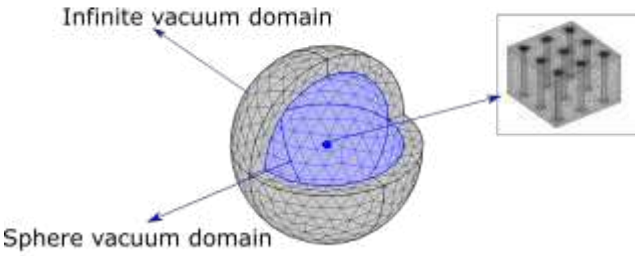

Figure 5. FEA model configuration and meshes (A quarter of the model is hidden to make the inner geometry visible).

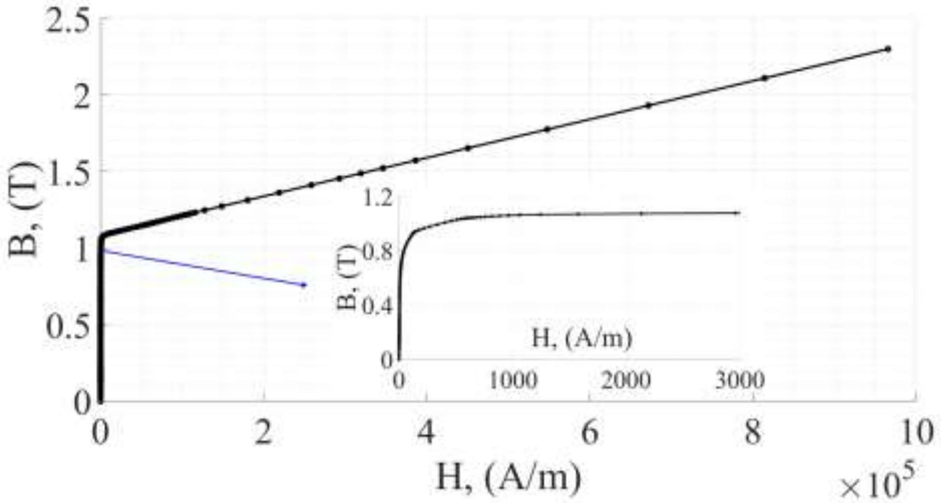

Figure 6. Permalloy B-H curve from the COMSOL material library [38,39].

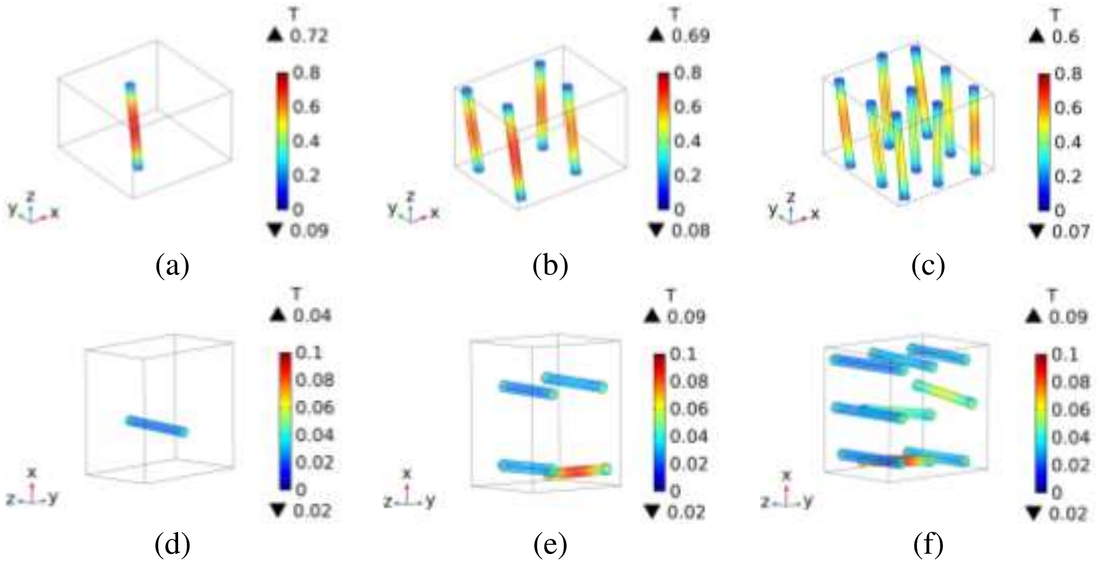

Figure 7. Flux density norm of Ni/Fe Z-pinned samples with 10000 A/m magnetic field applied: (a-c) out-of-plane (d-f) in-plane.

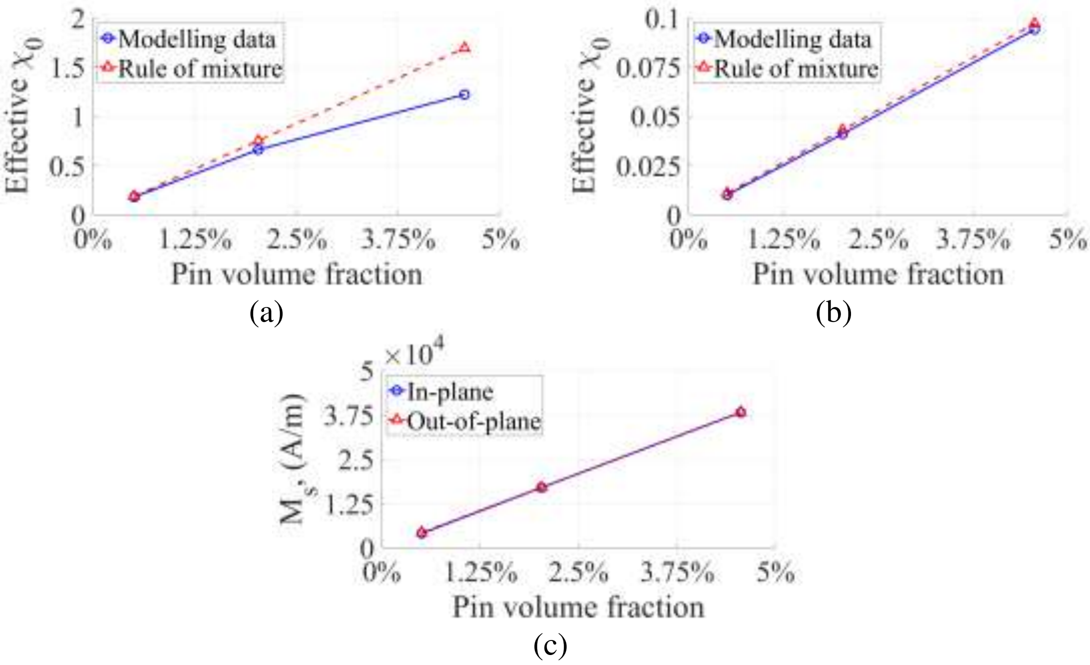

Figure 8. Modelling result of ideal Ni/Fe Z-pinned samples: (a) out-of-plane linear-part effective magnetic susceptibility against pin volume fraction, (b) in-plane linear-part effective magnetic susceptibility against pin volume fraction, (c) saturation magnetisation against pin volume fraction.

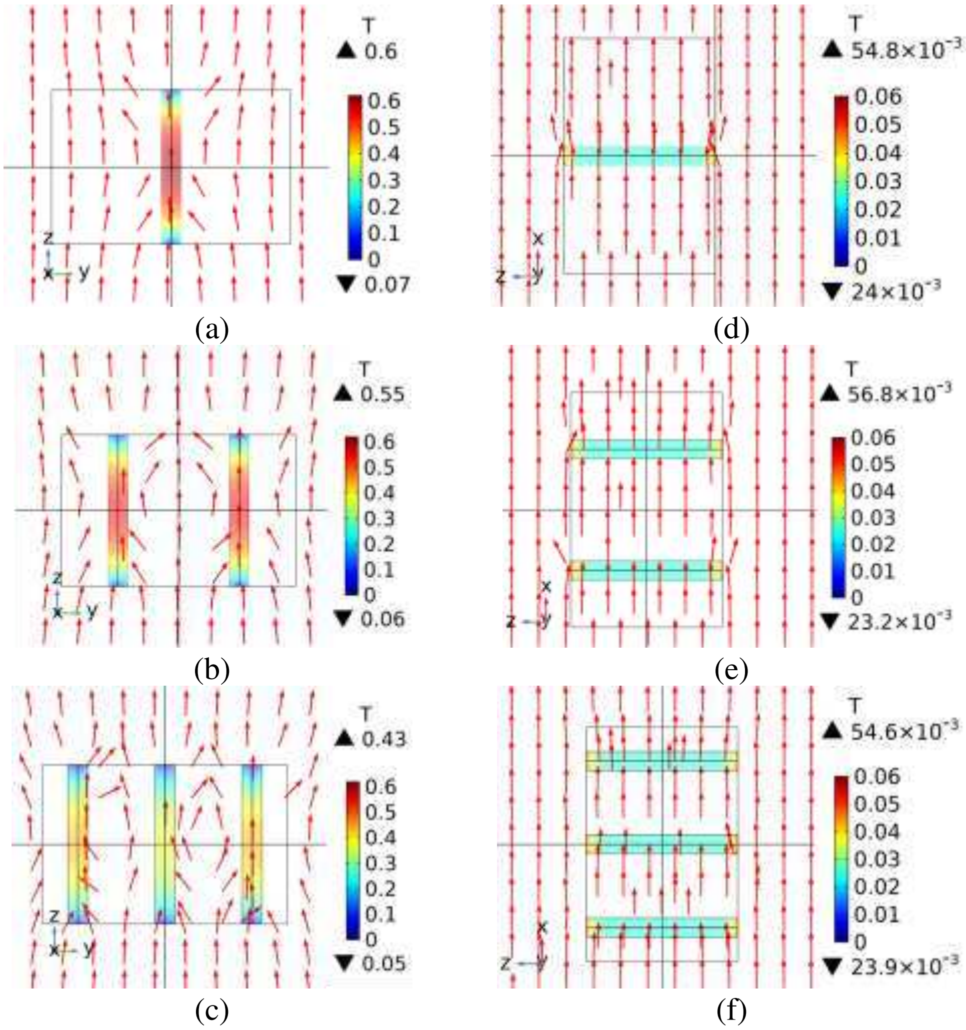

Figure 9. Cross section flux density norm of pins and distribution around them (modelling result of three ideal Ni/Fe Z-pinned samples with the 10000 A/m magnetic field applied): (a-c) out-of-plane (d-f) in-plane.

Supplementary document

Mudan Chen, Bing Zhang, Sven Friedemann, Giuliano Allegri, Stephen R. Hallett

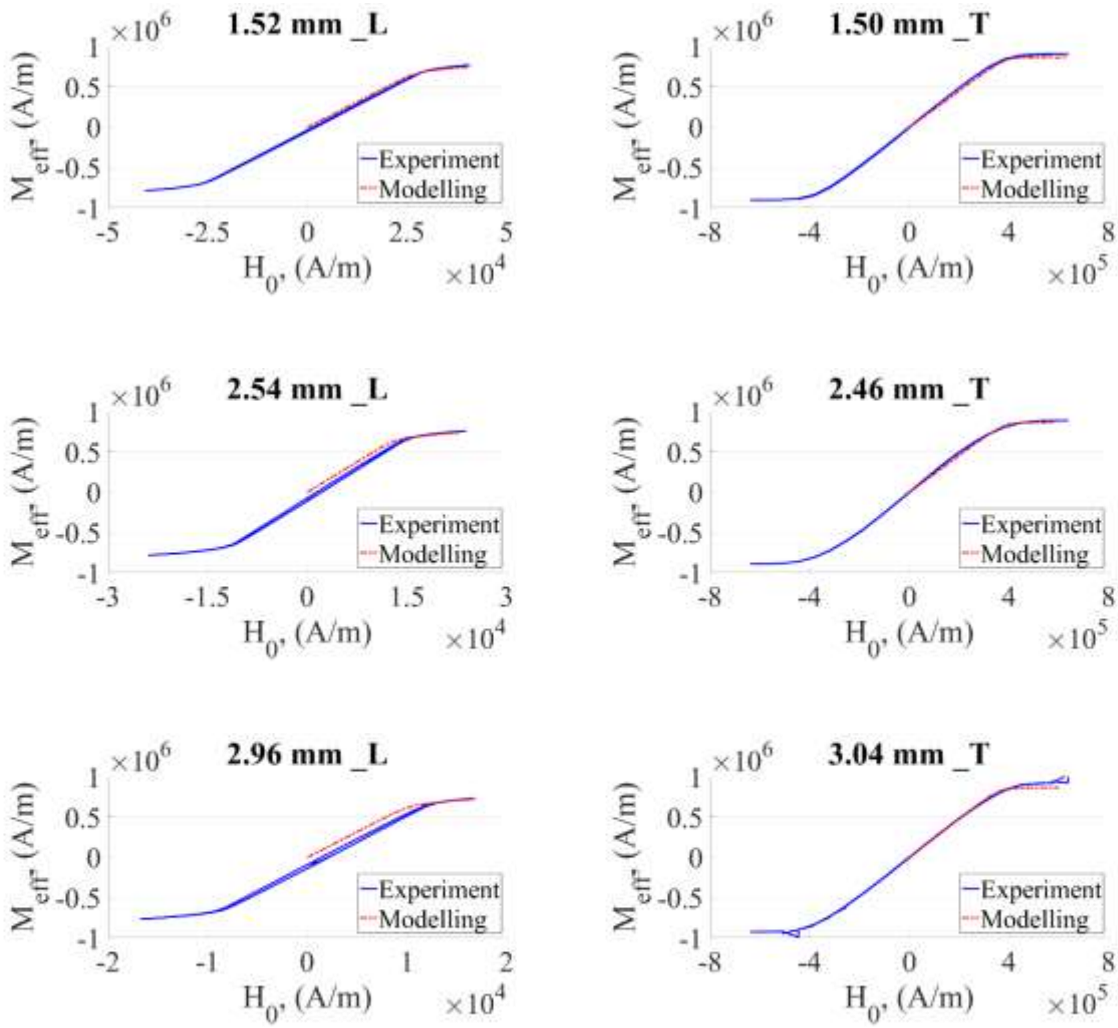

Figure S1. Comparison of experimental and modelling M-H curves of Ni/Fe pins with variable lengths (L: longitudinal, T: radial).

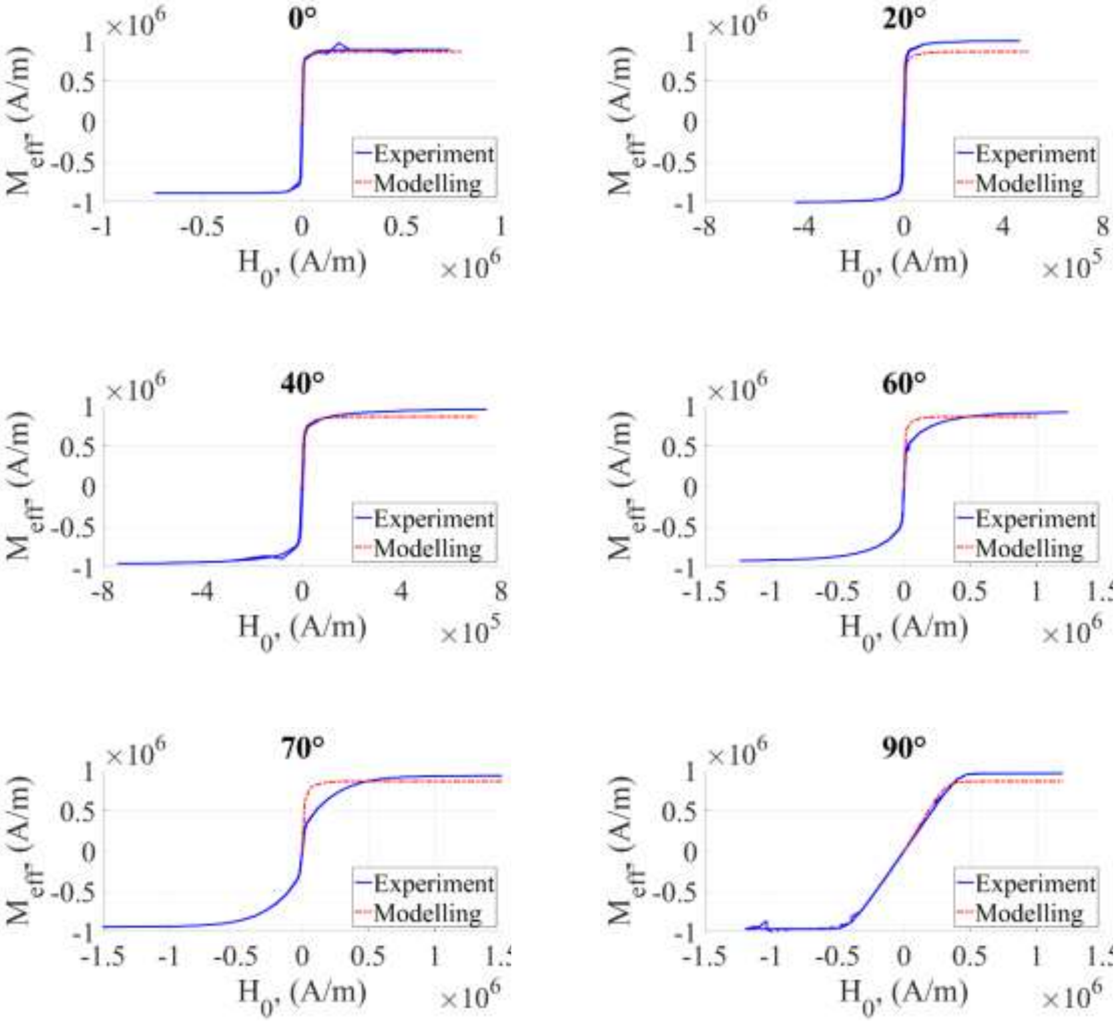

Figure S2. Comparison of experimental and modelling M-H curves of the single 4.05 mm long Ni/Fe alloy pin with variable inclination angles.

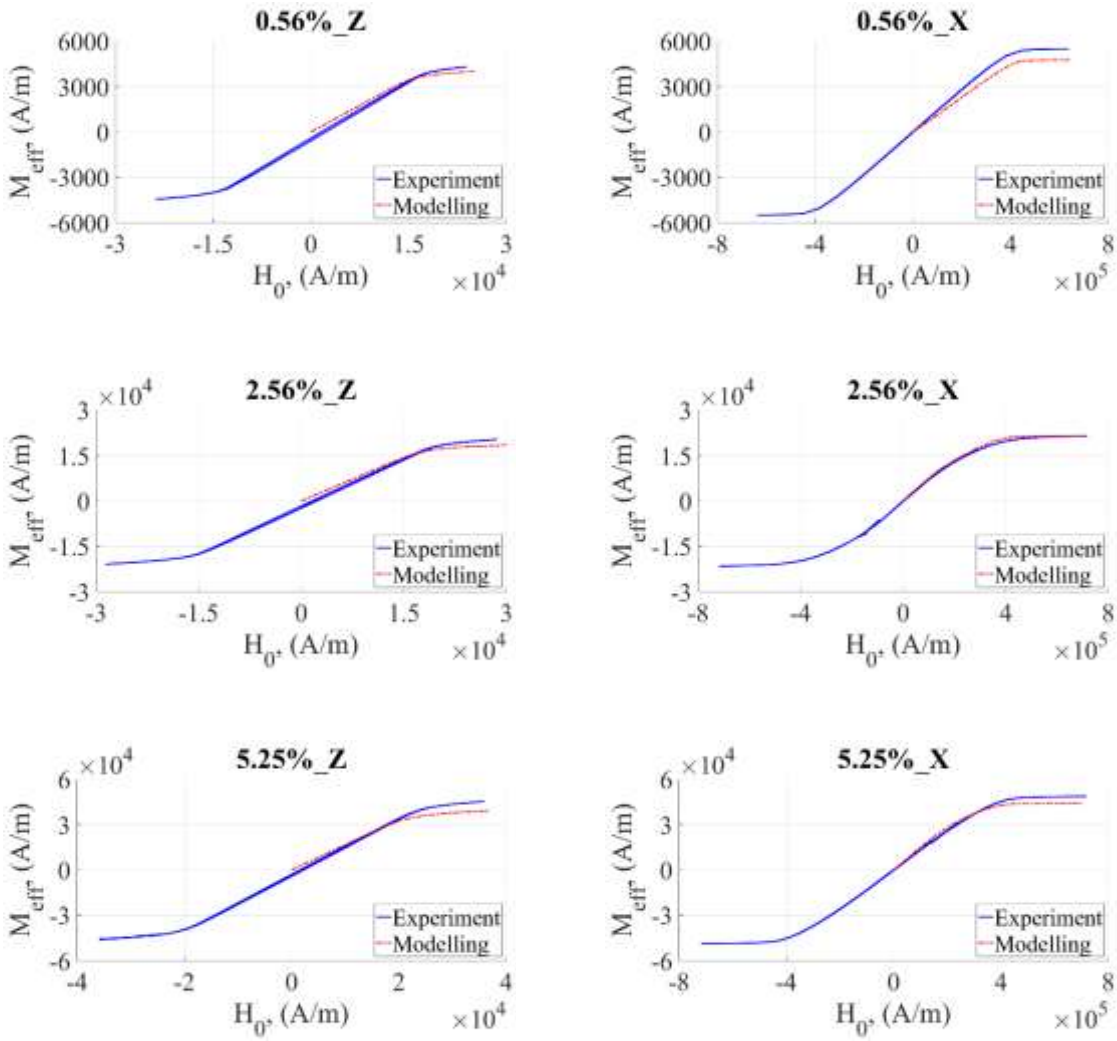

Figure S3. Comparison of experimental and modelling M-H curves of Ni/Fe pins reinforced laminate coupons (Z: out-of-plane, X: in-plane).